Research Square

Preprints are preliminary reports that have not undergone peer review.
They should not be considered conclusive, used to inform clinical practice,
or referenced by the media as validated information.

Energy and exergy trade-offs in heat and moisture recovery from humid return air in deep mines using low-temperature groundwater

Minhua Huang

huangm_h@163.com

Hunan University of Technology

Hongxin Jin[1]

Hunan University of Technology

Ke Yang[2]

Yunnan Land and Resources Vocational College

Can Li[1]

Hunan University of Technology

Aixiang Xu[1]

Hunan University of Technology

Shiqiang Chen[3]

Hunan University of Science and Technology

Research Article

Keywords: deep mine, groundwater cold source, dew-point crossing, finite-source effectiveness, exergy destruction

Posted Date: November 25th, 2026

DOI: https://doi.org/10.21203/rs.3.rs-11615625/v1

License: This work is licensed under a Creative Commons Attribution 4.0 International License.
Read Full License

Additional Declarations: No competing interests reported.

Energy and exergy trade-offs in heat and moisture recovery from humid return air in deep mines using low-temperature groundwater

Minhua Huang[1]*, Hongxin Jin[1], Ke Yang[2], Can Li[1], Aixiang Xu[1], Shiqiang Chen[3]

[1] School of Civil and Environmental Engineering, Hunan University of Technology, Zhuzhou 412000, Hunan Province, China
[2] Yunnan Land and Resources Vocational College, Kunming 652501, Yunnan Province, China
[3] College of Resource, Environment and Safety Engineering, Hunan University of Science and Technology, Xiangtan 411201, Hunan Province, China
*Corresponding author: Minhua Huang, huangm_h@163.com; ORCID: 0000-0002-9977-0974

Abstract: Deep-mine return air often combines high temperature and humidity, while mine groundwater offers a naturally available low-temperature sink. When the interface falls below the bulk-air dew point, direct air-water contact shifts from mainly sensible exchange to coupled cooling, condensation and latent-heat release. This study develops a one-dimensional two-film model with signed local vapor transfer, condensate mass conservation, interfacial energy balance, finite groundwater heat capacity and moist-air exergy accounting. A finite-source equilibrium limit and four regime descriptors are introduced. Without fitting outlet states, reconstruction of the ASHRAE parallel-flow air-washer benchmark yields a mean absolute relative deviation of 10.1% for four outlet descriptors, with a maximum deviation of 15.2% for humidity ratio. For 35 °C, 90% RH air contacting 18 °C groundwater, the model predicts an outlet air temperature of 31.51 °C, an outlet humidity ratio of 24.97 g·kg^{-1} dry air and a total heat-recovery rate of 23.56 kW, including an 18.97 kW latent contribution. Approximately 82.6% of moisture removal and 92.9% of exergy destruction occur within the first 40% of the contact length. Lowering groundwater temperature from 28 to 8 °C raises heat recovery from 8.36 to 37.55 kW but also increases exergy destruction from 0.08 to 1.69 kW. The results show that direct-contact recovery should be designed around finite-source matching and the spatial distribution of condensation rather than maximum cooling intensity alone.

Keywords: deep mine; groundwater cold source; dew-point crossing; finite-source effectiveness; exergy destruction

Nomenclature

Symbol	Definition	Unit
c_p	specific heat capacity	J·kg^{-1}·K^{-1}
C_r	air-to-water heat-capacity-rate ratio	–
e_x	specific flow exergy	kJ·kg^{-1}
h	specific enthalpy	J·kg^{-1}
h_{fg}	latent heat of vaporization/condensation	J·kg^{-1}
H_c	effective gas-side sensible conductance per axial length	W·m^{-1}·K^{-1}
H_m	effective vapor-transfer conductance per axial length	m^2·s^{-1}
H_w	effective liquid-side thermal conductance per axial length	W·m^{-1}·K^{-1}
j'_v	signed water-vapor transfer rate per unit axial length; positive for condensation	kg·m^{-1}·s^{-1}
L	effective contact length	m
$\dot{m}$	mass flow rate	kg·s^{-1}
p_v	water-vapor partial pressure	Pa
p_{vs}	saturation vapor pressure	Pa
$\dot{Q}_s$	effective sensible/non-phase-change	kW

Symbol	Definition	Unit
	contribution	
$\dot{Q}_l$	latent-heat contribution	kW
$\dot{Q}_t$	total air-side enthalpy recovery rate	kW
R	specific gas constant	J·kg^{-1}·K^{-1}
T	temperature	°C or K as indicated
T_{dp}	dew-point temperature	°C
T_{eq}	finite-source equilibrium temperature	°C
x	axial coordinate	m
χ_c	condensation-zone fraction	–
$\eta_{\mathrm{h},\infty}$	inlet-water/infinite-reservoir enthalpy efficiency	–
$\varepsilon_{\mathrm{h},f}$	finite-source enthalpy effectiveness	–
Λ	latent-potential ratio	–
Π_{dp}	dew-point-crossing potential number	–
Π_L	latent-dominance factor	–
Π_D	exergy-degradation number	–
ϕ	relative humidity	–
ρ_v	water-vapor density	kg·m^{-3}
ω	humidity ratio	kg·kg^{-1} dry air

Subscripts: a, air; w, liquid water; i, interface; v, water vapor; da, dry air; in, inlet; out, outlet; 0, environmental reference state; *sat*, saturated state; *t*h, thermal; *c*h, humidity/chemical component.

1. Introduction

As mineral extraction extends to greater depths, the underground thermal environment is increasingly controlled by the combined effects of surrounding-rock heat release, electromechanical equipment, compression and ventilation work, hot-water seepage, and long ventilation routes [1–6]. The resulting return air is not simply "hot air". In many deep mines it is simultaneously hot and humid, and its total enthalpy can contain a large latent component associated with water vapor [7–10]. This distinction is important because sensible-temperature control alone does not reveal either the amount of recoverable heat and moisture or the thermodynamic quality of that recovered energy.

A range of engineering approaches has been investigated for deep-mine heat-hazard mitigation, including increased ventilation, refrigeration, surface cooling, spray cooling and mine-water-source systems [4,5,15,17,18,28,29]. Groundwater is particularly attractive because it is already present in many mines and can be substantially colder than the return air. If the water temperature is above the air dew point, water and air exchange primarily sensible heat and, depending on the local vapor-pressure difference, may even undergo evaporation. Once the local interfacial temperature falls below the vapor-equilibrium temperature of the bulk air, however, the transfer path changes qualitatively: vapor diffuses toward the interface, condenses, and releases latent heat. Similar coupled heat-and-mass-transfer phenomena are central to dehumidifiers, air washers, cooling towers and direct-contact condensers [8,11–14,19–23].

The first-law description of such processes is relatively mature. Psychrometric enthalpy, humidity ratio, transfer coefficients and condensate rates can be used to quantify the reduction in the air-side heat and moisture load [7,8,19–22]. The difficulty lies in determining how much of the recovered energy remains thermodynamically useful. Qureshi and Zubair [10] showed that exergy analysis can reveal limitations hidden by conventional psychrometric energy analysis. Zhang et al. [23] separated thermal and humidity-related exergy behavior in coupled humid-air/water transfer and demonstrated that irreversibility cannot necessarily be

removed by increasing transfer area. Their later unified treatment further clarified exergy flow and destruction during direct contact between humid air and water or liquid-desiccant solution [9]. Related exergy analyses of air cooling and dehumidification systems likewise show that energy removal and exergy performance can respond differently to operating conditions [24–27]. Therefore, simply establishing another energy-plus-exergy balance is insufficient as a contribution by itself.

Three issues remain especially relevant to deep-mine groundwater utilization. First, the inlet condition $T_{w,in}<T_{dp,in}$ is only a potential criterion. Actual condensation is local and depends on the evolving difference between bulk vapor pressure and saturation vapor pressure at the interface. A model should therefore allow the vapor-transfer rate to change sign rather than prescribing condensation throughout the entire contactor. Second, mine groundwater is a finite-capacity stream that warms continuously. Defining the theoretical maximum air-side enthalpy reduction as cooling the air to the saturated state at $T_{w,in}$ implicitly treats the water as an infinite isothermal reservoir and can substantially overstate the physically accessible recovery potential. Third, direct-contact condensation is strongly non-uniform along the flow direction. Large temperature and vapor-pressure differences at the inlet can localize both useful transfer and irreversible degradation upstream, so total heat transfer alone provides little guidance for contactor length, staged water distribution or flow arrangement.

Accordingly, this work focuses on the dew-point-crossing mechanism and finite-source thermodynamic limit of direct contact between deep-mine humid air and low-temperature groundwater. The contributions are fourfold. (1) A signed two-film formulation is established in which condensation and evaporation are determined by the local vapor-density difference, and condensate mass is explicitly added to the liquid stream. (2) A finite-source equilibrium temperature is derived from the coupled mass and energy balances, providing a physically attainable reference limit in addition to the conventional inlet-water reference. (3) The condensation-zone fraction and inlet regime descriptors are introduced to connect dew-point crossing with the spatial distribution of latent transfer. (4) The energy-exergy trade-off is quantified for variations in groundwater temperature and inlet air humidity, with emphasis on engineering implications for deep-mine heat and moisture recovery.

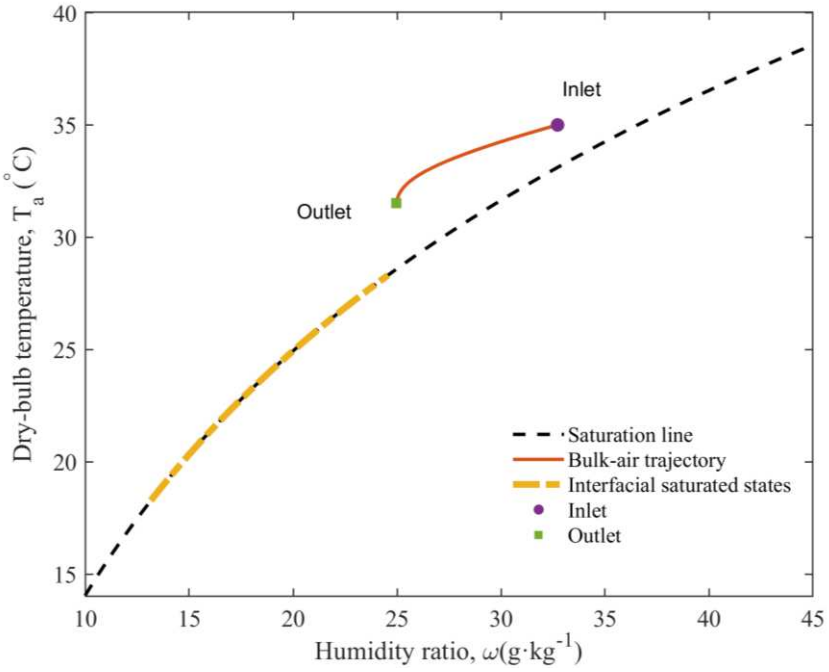

Figure 1. Psychrometric trajectory of the bulk humid air and the corresponding interfacial saturated states during dew-point-crossing direct contact under the baseline condition.

2. Engineering context and physical model

2.1 Physical process

Figure 1 provides a thermodynamic interpretation of the direct-contact process. The bulk humid-air state moves from the inlet condition toward lower temperature and lower humidity ratio, while the local interfacial

state remains on the saturation locus determined by the interfacial temperature. The finite separation between the bulk-air trajectory and the interfacial saturated-state trajectory represents the simultaneous thermal and vapor-transfer driving forces. This representation is particularly useful under dew-point-crossing conditions because the air does not follow either a constant-humidity-ratio line or the saturation curve; instead, its path is governed by the coupled response of sensible cooling, vapor diffusion, condensation, and finite warming of the groundwater cold source.

At an arbitrary axial position x, the bulk air state is described by T_a and ω, the bulk water by T_w, and the interface by T_i. Local interfacial vapor equilibrium is assumed, so the vapor pressure immediately at the interface is $p_{vs}(T_i)$. The bulk-air vapor pressure, by contrast, is determined by the instantaneous humidity ratio. A positive difference $p_{v,a}$-$p_{vs}(T_i)$ drives condensation; a negative difference drives evaporation. This local criterion is more rigorous than assuming that the entire contactor condenses whenever the inlet water temperature is below the inlet dew point.

The psychrometric path in Fig. 1 is therefore not constrained to either a constant-humidity line or the saturation line. The bulk air moves continuously toward the local interfacial equilibrium state while the water simultaneously warms, so the interface itself also moves through state space. This coupled movement is the origin of the rapidly decaying mass-transfer driving force observed downstream.

2.2 Modeling assumptions and scope

The following assumptions are adopted to isolate the thermodynamic mechanism. Moist air is treated as an ideal mixture of dry air and water vapor. Liquid water is incompressible and its specific heat is constant over the investigated temperature range. The process is steady and one-dimensional in the mean-flow direction. External heat loss, shaft work, kinetic-energy change and potential-energy change are neglected. The total pressure is constant at 101.325 kPa. The local gas-liquid interface is in vapor equilibrium, but the bulk gas and liquid are not. Condensed water immediately joins the liquid stream, and its mass and enthalpy are therefore included in the liquid-side conservation equations. Droplet entrainment, water chemistry, dissolved gases, pressure drop, transient film accumulation and multidimensional interfacial deformation are not resolved.

The parameters H_c, H_m and H_w are effective per-length transfer conductances. They contain the influence of local interfacial area and geometry. Holding them constant allows the present study to separate the thermodynamic effects of inlet humidity and water temperature from geometry-specific correlations. They are **not universal coefficients** and must be replaced by experimentally identified or geometry-resolved correlations before the model is used for quantitative design of a specific mine contactor.

3. Thermodynamic and transport formulation

3.1 Moist-air properties and local phase-change criterion

The saturation vapor pressure is calculated using the Buck equation [30]:

$$p_{vs}(T)=611.21\exp\left[\left(18.678-\frac{T}{234.5}\right)\frac{T}{257.14+T}\right] \quad (1)$$

where T is in °C and p_{vs} is in Pa. The humidity ratio is:

$$\omega=0.621945\frac{p_v}{P-p_v}, \qquad p_v=P\frac{\omega}{0.621945+\omega} \quad (2)$$

and the specific enthalpy of moist air per unit mass of dry air is written in SI form as:

$$h_a=c_{p,da}T_a+\omega\left(h_{fg,0}+c_{p,v}T_a\right) \quad (3)$$

The inlet dew-point temperature satisfies:

$$p_{vs}\left(T_{dp,in}\right)=p_{v,in} \quad (4)$$

At the interface:

$$\rho_{v,a}=\frac{p_{v,a}}{R_v(T_a+273.15)}, \qquad \rho_{v,i}=\frac{p_{vs}(T_i)}{R_v(T_i+273.15)} \tag{5}$$

The signed vapor-transfer rate per unit axial length is defined as:

$$j'_v=\mathrm{H}_m\left(\rho_{v,a}-\rho_{v,i}\right) \tag{6}$$

Thus $j'_v>0$ denotes condensation from air to water, $j'_v=0$ denotes local vapor equilibrium and $j'_v<0$ denotes evaporation. Equation (6) provides the actual local phase-change criterion used by the numerical model.

For a convenient inlet-level measure of dew-point crossing, the potential number is defined as:

$$\Pi_{dp}=\frac{T_{dp,in}-T_{w,in}}{T_{a,in}-T_{w,in}} \tag{7}$$

For the present cooling problem, $\Pi_{dp}\leq 0$ means that the inlet water does not cross the inlet dew point; $0<\Pi_{dp}<1$ indicates increasing condensation potential as Π_{dp} approaches unity. Because $T_i\neq T_w$ and both states evolve, Eq. (7) is a regime descriptor rather than a substitute for the local criterion in Eq. (6).

3.2 Interfacial energy balance and governing equations

The sensible heat-transfer rate per unit axial length from bulk air to the interface is:

$$q'_s=\mathrm{H}_c(T_a-T_i) \tag{8}$$

At the interface, sensible transfer from the gas and latent heat released or absorbed by phase change are balanced by heat transfer to the liquid:

$$\mathrm{H}_c(T_a-T_i)+j'_v[h_v(T_i)-h_l(T_i)]=\mathrm{H}_w(T_i-T_w) \tag{9}$$

The vapor and liquid specific enthalpies, referenced to liquid water at 0 °C, are approximated by:

$$h_v(T)=h_{fg,0}+c_{p,v}T, \qquad h_l(T)=c_{p,w}T \tag{10}$$

Equation (9) is solved iteratively for T_i at every axial location. Because j'_v is signed, the same equation remains valid during either condensation or evaporation.

The dry-air mass flow rate is constant, whereas the vapor and liquid-water flow rates exchange mass. The humidity-ratio balance is:

$$\dot{m}_{da}\frac{d\omega}{dx}=-j'_v \tag{11}$$

The air-side energy balance is:

$$\dot{m}_{da}\frac{d\mathrm{h}_a}{dx}=-\mathrm{H}_c(T_a-T_i)-j'_v\mathrm{h}_v(T_i) \tag{12}$$

The liquid mass balance is:

$$\frac{d\dot{m}_w}{dx}=j'_v \tag{13}$$

and the liquid-stream energy balance is:

$$\frac{d[\dot{m}_w h_l(T_w)]}{dx}=\mathrm{H}_c(T_a-T_i)+j'_v h_v(T_i) \tag{14}$$

Equations (11)–(14) conserve both water mass and total energy. Expanding Eq. (14) gives the temperature equation used in the numerical solution:

$$\frac{dT_w}{dx}=\frac{\mathrm{H}_c(T_a-T_i)+j'_v[h_v(T_i)-h_l(T_w)]}{\dot{m}_w c_{p,w}} \tag{15}$$

The total air-side recovery rate is obtained directly from the moist-air enthalpy decrease:

$$\dot{Q}_t=\dot{m}_{da}\left(h_{a,in}-h_{a,out}\right) \tag{16}$$

The latent contribution is evaluated from the local phase-change term:

$$\dot{Q}_l=\int_0^L j'_v[h_v(T_i)-h_l(T_i)]dx, \qquad \dot{Q}_s=\dot{Q}_t-\dot{Q}_l \tag{17}$$

The latent-dominance factor is:

$$\Pi_L=\frac{\dot{Q}_l}{\dot{Q}_s} \tag{18}$$

For condensation cases, $\Pi_L>1$ indicates that phase-change energy exceeds the remaining non-latent contribution.

To characterize the inlet potential for latent transfer independently of the realized contactor performance, a latent-potential ratio is further defined as:

$$\Lambda=\frac{h_{fg,0}\max\left\{\omega_{in}-\omega_{sat}\left(T_{w,in}\right),0\right\}}{\left(c_{p,da}+\omega_{in}c_{p,v}\right)\left(T_{a,in}-T_{w,in}\right)} \tag{19}$$

$\Lambda>1$ means that the potential latent load associated with bringing the air toward saturation at the inlet-water temperature exceeds the sensible cooling scale.

3.3 Condensation-zone fraction

The local nature of Eq. (6) allows the fraction of the effective contact length that actually operates in the condensation regime to be quantified as

$$\chi_c=\frac{1}{L}\int_0^L I_c\,(x)\,dx \tag{20}$$

Here $I_c(x)=1$ when $j'_v(x)>j'_{v,\mathrm{tol}}$ and $I_c(x)=0$ otherwise. Unlike a total condensate rate, χ_c indicates whether the entire contactor is active or whether the downstream section has approached vapor equilibrium and provides little additional dehumidification. A small positive numerical tolerance $j'_{v,\mathrm{tol}}=10^{-10}$ kg·m^{-1}·s^{-1} is used only to prevent round-off noise from being classified as a finite condensation zone; changing this tolerance by one order of magnitude does not affect the reported maps.

3.4 Conventional and finite-source enthalpy limits

A common direct-contact reference assumes that the air could ideally leave saturated at the **inlet water temperature**. The corresponding maximum is:

$$\dot{Q}_{max,\infty}=\dot{m}_{da}\left[h_{a,in}-h_{sat}\left(T_{w,in}\right)\right], \qquad \eta_{\mathrm{h},\infty}=\frac{\dot{Q}_t}{\dot{Q}_{max,\infty}} \tag{21}$$

This reference is useful for comparison but implicitly treats the cold water as an infinite isothermal sink. In a real mine-water stream, however, the water warms and its mass can increase through condensation. In the limit of infinite transfer area, the two outlet streams approach a common equilibrium temperature T_{eq}; for the condensing cases considered here, the air is saturated at this equilibrium state. Define the inlet and equilibrium enthalpy-flow rates as:

$$\dot{H}_{in}=\dot{m}_{da}h_a\left(T_{a,in},\omega_{in}\right)+\dot{m}_{w,in}h_l\left(T_{w,in}\right) \tag{22}$$

$$\dot{H}_{eq}=\dot{m}_{da}h_{sat}\left(T_{eq}\right)+\left\{\dot{m}_{w,in}+\dot{m}_{da}\left[\omega_{in}-\omega_{sat}\left(T_{eq}\right)\right]\right\}h_l\left(T_{eq}\right) \tag{23}$$

Overall mass and energy conservation then require:

$$\dot{H}_{in}=\dot{H}_{eq} \tag{24}$$

Solving Eq. (24) gives the finite-source equilibrium state. The physically attainable finite-source maximum and effectiveness are then:

$$\dot{Q}_{max,f}=\dot{m}_{da}\left[h_{a,in}-h_{sat}\left(T_{eq}\right)\right], \qquad \varepsilon_{\mathrm{h},f}=\frac{\dot{Q}_t}{\dot{Q}_{max,f}} \tag{25}$$

The distinction between $\eta_{\mathrm{h},\infty}$ and $\varepsilon_{\mathrm{h},f}$ is central to the present analysis: the former measures recovery relative to an idealized constant-temperature reservoir, whereas the latter measures utilization of the finite cold-source capacity that is actually available.

3.5 Moist-air exergy and overall exergy destruction

The environmental reference state is set to T_0=298.15 K, P_0=101.325 kPa and ϕ_0=0.60. For constant system pressure $P=P_0$, the mechanical exergy term vanishes. Following established moist-air exergy formulations [9,10,23], the specific exergy per unit mass of dry air is written as:

$$e_a=e_{a,\mathrm{th}}+e_{a,\mathrm{ch}} \tag{26}$$

With thermal and humidity/composition contributions:

$$e_{a,\mathrm{th}}=\left(c_{p,da}+\omega c_{p,v}\right)\left[T_K-T_0-T_0\ln\left(\frac{T_K}{T_0}\right)\right] \tag{27}$$

$$e_{a,\mathrm{ch}}=R_{da}T_0\left[(1+1.608\omega)\ln\left(\frac{1+1.608\omega_0}{1+1.608\omega}\right)+1.608\omega\ln\left(\frac{\omega}{\omega_0}\right)\right] \tag{28}$$

Here T_{K} is in kelvin and ω_0 is the humidity ratio of the reference environment. The liquid-water stream requires both a thermal contribution and a chemical contribution because liquid water is not in chemical equilibrium with an unsaturated environmental vapor. Neglecting pressure exergy, its specific exergy is:

$$e_w=c_{p,w}\left[T_{w,K}-T_0-T_0\ln\left(\frac{T_{w,K}}{T_0}\right)\right]+R_vT_0\ln\left(\frac{p_{vs}(T_0)}{p_{v,0}}\right) \tag{29}$$

where $p_{v,0}=\phi_0 p_{vs}(T_0)$; therefore, the second term is equivalently $-R_vT_0\ln\phi_0$. The chemical term is retained because water is transferred between the vapor and liquid streams; omitting it can produce an artificial exergy imbalance as the local regime approaches evaporation. In Eqs. (26)–(29), heat capacities and gas constants are expressed in kJ·kg^{-1}·K^{-1} so that e_a and e_w are obtained in kJ·kg^{-1}. For the adiabatic control volume with no shaft work, the overall exergy-destruction rate is:

$$\dot{E}_D=\dot{m}_{da}e_{a,in}+\dot{m}_{w,in}e_{w,in}-\dot{m}_{da}e_{a,out}-\dot{m}_{w,out}e_{w,out} \tag{30}$$

The cumulative value up to an arbitrary axial location is evaluated by applying Eq. (30) to the partial control volume from the inlet to x. A dimensionless exergy-degradation number is defined as:

$$\Pi_D=\frac{\dot{E}_D}{\dot{Q}_t} \tag{31}$$

Π_D is not an exergy efficiency; it measures the irreversible exergy destruction associated with each unit of recovered air-side enthalpy. It is reported only for heat-recovery states with $\dot{Q}_t>0$.

4. Numerical implementation and model verification

4.1 Baseline conditions and numerical solution

The coupled governing equations were solved in MATLAB using the adaptive Runge–Kutta solver ode45. At each right-hand-side evaluation, Eq. (9) was solved for T_i using a bracketed scalar root-finding procedure. The state vector was $\mathbf{y}=[h_a,\omega,T_w,\dot{m}_w]^T$. The relative tolerance was 2×10^{-8}, and the corresponding absolute tolerances for the four state variables were 10^{-5}J·kg^{-1}, 10^{-11}, 10^{-9}°C and 10^{-11}kg·s^{-1}, respectively. Numerical accuracy was checked through total-water-mass and overall-energy closure, both of which were negligible relative to the reported transfer rates.

Table 1. Baseline calculation conditions

Parameter	Value
Inlet air temperature, $T_{a,in}$	35 °C
Inlet air relative humidity, ϕ_{in}	0.90
Inlet humidity ratio, ω_{in}	32.72 g·kg⁻¹ dry air
Inlet groundwater temperature, $T_{w,in}$	18 °C
Dry-air flow rate, $\dot{m}_{da}$	1.000 kg·s⁻¹
Inlet liquid-water flow rate, $\dot{m}_{w,in}$	0.525 kg·s⁻¹
Effective contact length, L	5.0 m
H_c	110.43 W·m⁻¹·K⁻¹
H_m	0.2992 m²·s⁻¹
H_w	6.0499×10^4 W·m⁻¹·K⁻¹
Total pressure, P	101.325 kPa
Exergy reference state	25 °C, 101.325 kPa, 60% RH

4.2 External benchmark verification and experimental trend consistency

The governing equations were first checked against the parallel-flow air-washer design example reported in the ASHRAE Handbook [31]. This benchmark is deliberately useful because it operates in the opposite transfer direction from the main mine-cooling cases: hot water heats and humidifies cooler air, so the signed formulation must predict evaporation ($j'_v<0$) without changing the governing equations. The benchmark specifies $T_{w,in}$=35 °C, $T_{a,in}$=18.3 °C, inlet wet-bulb temperature 7.2 °C, dry-air mass flux 1.628 kg·m^{-2}·s^{-1}, liquid-to-air spray ratio 0.70, $h_a a_H$=1.34 kW·m^{-3}·K^{-1} , $h_L a_H$=16.77 kW·m^{-3}·K^{-1}, cross-sectional area 2.26 m^2, and chamber length 1.19 m. The reference outlet state is $T_{a,out}$=22.4 °C, $T_{w,out}$=23.9 °C and $h_{a,out}$=73.6 kJ·kg^{-1} dry air [31].

For this check, the effective per-length thermal conductances are obtained directly from the reported volumetric coefficients, $H_c=(h_a a_H)A_{cs}$ and $H_w=(h_L a_H)A_{cs}$. The vapor-transfer conductance is converted from the Lewis relation using the reported dry-air density and the inlet humid specific heat. No outlet quantity is used for parameter fitting. Table 2 shows that the model reproduces the benchmark outlet air temperature, water temperature and moist-air enthalpy within 6.1%, 10.4% and 8.6%, respectively. The humidity-ratio deviation is larger (15.2%), which reflects differences between the present vapor-density driving-force formulation and the enthalpy-potential/Lewis approximation used in the handbook design method. The mean absolute relative deviation of the four outlet descriptors is 10.1%.

Table 2. External benchmark against the ASHRAE parallel-flow air-washer example [31].

Outlet quantity	ASHRAE reference	Present model	Relative deviation
$T_{a,out}$ (°C)	22.40	23.76	+6.1%
$T_{w,out}$ (°C)	23.90	26.38	+10.4%

Outlet quantity	ASHRAE reference	Present model	Relative deviation
ω_{out} (g·kg^{-1} dry air)	20.08	17.03	-15.2%
$h_{a,out}$ (kJ·kg^{-1} dry air)	73.60	67.24	-8.6%

Independent experiments provide an additional directional check for the condensation regime. Yoo and Kwon [32] reported that, during direct-contact cooling, lower inlet water temperature and larger water flow reduce both outlet air temperature and humidity ratio. Karameldin et al. [33] observed in a co-current spray direct-contact condenser that condensate production increases with humid-air thermal/moisture loading and with cooled-water mass flux, with diminishing benefit at sufficiently high liquid flux. These experimentally observed response directions are reproduced by the present model. Because the published apparatuses differ substantially from the mine-contact configuration and do not provide all coefficients needed for a one-to-one geometry-resolved reconstruction, they are used as trend validation rather than as additional fitted datasets.

4.3 Conservation checks and limiting behavior

The baseline values of H_c, H_m and H_w in Table 1 are effective reference conductances used to isolate thermodynamic effects; they are not claimed as universal properties of a spray, packed bed or wetted-string-grid contactor. This distinction is important because the absolute outlet state of a particular device depends on interfacial area, hydrodynamics and geometry-specific *Nu*/*Sh* correlations. To determine whether the principal conclusions are artifacts of the selected reference conductances, each conductance was varied independently from 0.5 to 2.0 times its baseline value while all inlet conditions were fixed.

Over this range, the total recovered heat remains within -8.4% to +3.4% of the baseline and the condensate rate within -13.4% to +3.8%. The response is most sensitive to H_m, as expected for a latent-dominated process, whereas varying H_w from 0.5 to 2.0 changes $\dot{Q}_t$ by less than 0.1%, confirming that the adopted baseline represents a small liquid-side thermal resistance. The direction of the groundwater-temperature and inlet-humidity effects, the upstream localization of condensation, and the finite-source limiting behavior remain unchanged. Accordingly, the reported absolute values should be interpreted as reference calculations, while the regime transitions and normalized trends are the principal generalizable results. Device-scale design requires replacement of the effective conductances by measured or geometry-resolved transfer correlations.

5. Results and discussion

5.1 Axial localization of coupled heat and moisture transfer

For the baseline state of $T_{a,in}$=35 °C, ϕ_{in}=0.90 and $T_{w,in}$=18 °C, the inlet dew-point temperature is approximately 33.1 °C, which is substantially higher than the groundwater temperature. The calculation therefore starts in a strong dew-point-crossing regime. Although the outlet dry-bulb temperature decreases by only about 3.5 °C, the humidity ratio decreases by approximately 7.8 g kg^{-1} dry air. The corresponding total recovered heat is about 23.6 kW, of which approximately 19.0 kW is associated with the latent contribution. Thus, the baseline process is clearly latent-dominated rather than being describable as conventional sensible cooling.

The four panels in Fig. 2 show that the underlying transport fields are highly non-uniform along the contact length. The interfacial temperature remains between the bulk-air and groundwater temperatures, while the gap between the bulk humidity ratio and the interfacial equilibrium humidity ratio contracts progressively downstream. The local vapor-pressure difference and condensation flux are therefore largest close to the inlet and decay rapidly as the two phases approach local equilibrium. The cumulative representation further demonstrates that moisture removal and exergy destruction are disproportionately concentrated in the upstream section. This finding means that geometrical contact length and thermodynamically active contact length are not equivalent: once the local vapor-pressure driving force has largely collapsed, additional downstream area contributes only marginally to dehumidification.

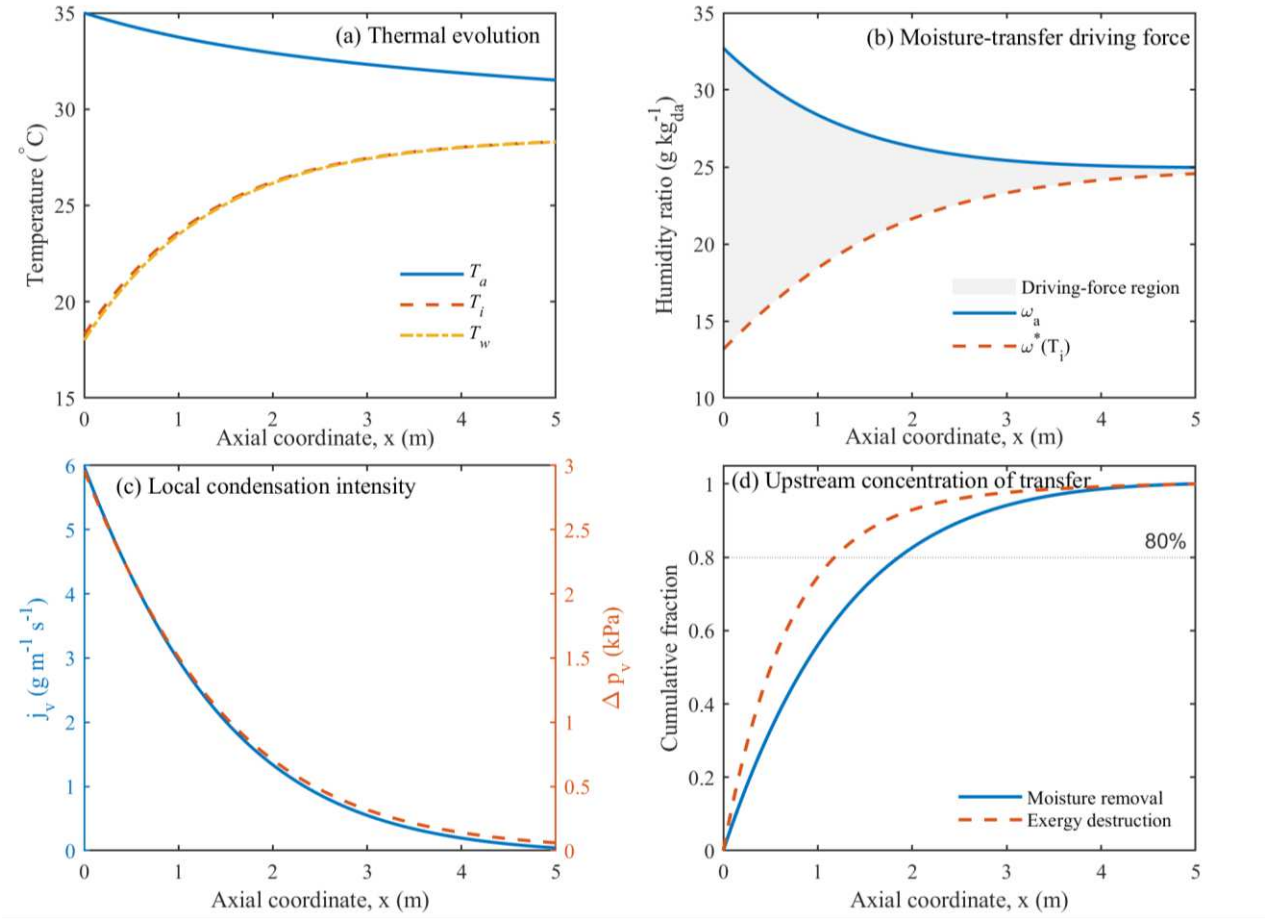

Figure 2. Axial evolution of (a) air, interface and groundwater temperatures, (b) bulk and interfacial equilibrium humidity ratios, (c) condensation mass flux and vapor-pressure driving force, and (d) cumulative moisture removal and exergy destruction under the baseline condition.

5.2 Finite-source limiting behavior and conductance sensitivity

A central distinction of the present formulation is that groundwater is treated as a finite-capacity cold source rather than an isothermal reservoir. Figure 3(a) demonstrates that, as the three effective conductances are increased by a common multiplier, the outlet air and water temperatures converge toward a common finite-source equilibrium temperature instead of toward the inlet water temperature. For the baseline condition, the calculated equilibrium temperature is approximately 28.9 °C and $\varepsilon_{h,f}$ approaches unity as the conductance multiplier becomes large. This limiting behavior is obtained while satisfying the total water-mass and energy balances, providing a stringent internal check on the coupled formulation.

The finite-source correction materially changes the interpretation of performance. Using the inlet water temperature as an infinite-reservoir reference gives a conventional enthalpy efficiency of only about 0.35 for the baseline case, whereas the finite-source effectiveness is approximately 0.95. The former metric therefore exaggerates the apparent unused recovery potential because it ignores warming of the groundwater and the associated movement of the equilibrium state.

Figure 3(b) quantifies the conductance sensitivity discussed in Section 4.3. Halving H_m produces the largest reduction in total recovery and condensate generation, whereas increasing it above the baseline gives progressively smaller gains as the gas and liquid states approach local equilibrium. Variation of H_c mainly redistributes sensible and latent contributions but changes $\dot{Q}_t$ by only a few percent over the tested range.These results support the use of the model for regime and mechanism analysis while reinforcing that apparatus-specific conductances are required for quantitative equipment design.

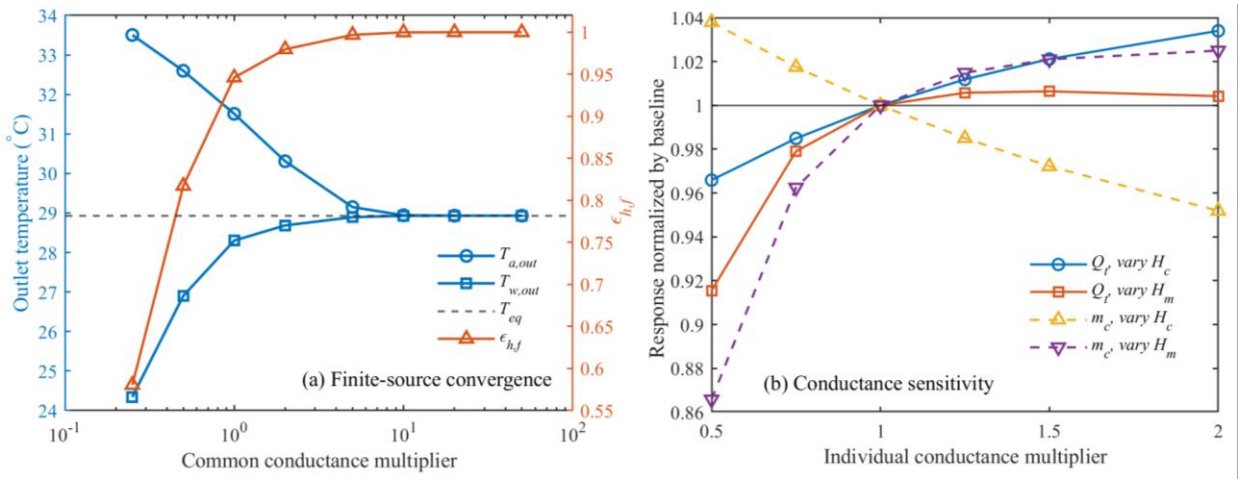

Figure 3. Model limiting behavior and parameter robustness: (a) convergence of outlet air and groundwater temperatures toward the finite-source equilibrium temperature, together with $\varepsilon_{h,f}$, as all transfer conductances are increased by a common multiplier; and (b) normalized sensitivity of total recovered heat and condensate rate to independent variation of H_c and H_m.

5.3 Influence of inlet groundwater temperature

Figure 4 shows that inlet groundwater temperature controls both the magnitude and the composition of the recovered energy. Decreasing $T_{w,in}$ from 28 to 8 °C increases the total recovered heat from approximately 8.4 to 37.6 kW. The latent contribution rises from about 6.3 to 30.5 kW and remains greater than the sensible contribution over the investigated range. The stacked representation in Fig. 4(a) makes clear that colder groundwater does not merely increase the sensible temperature difference; it also deepens the dew-point crossing and thereby strengthens condensation.

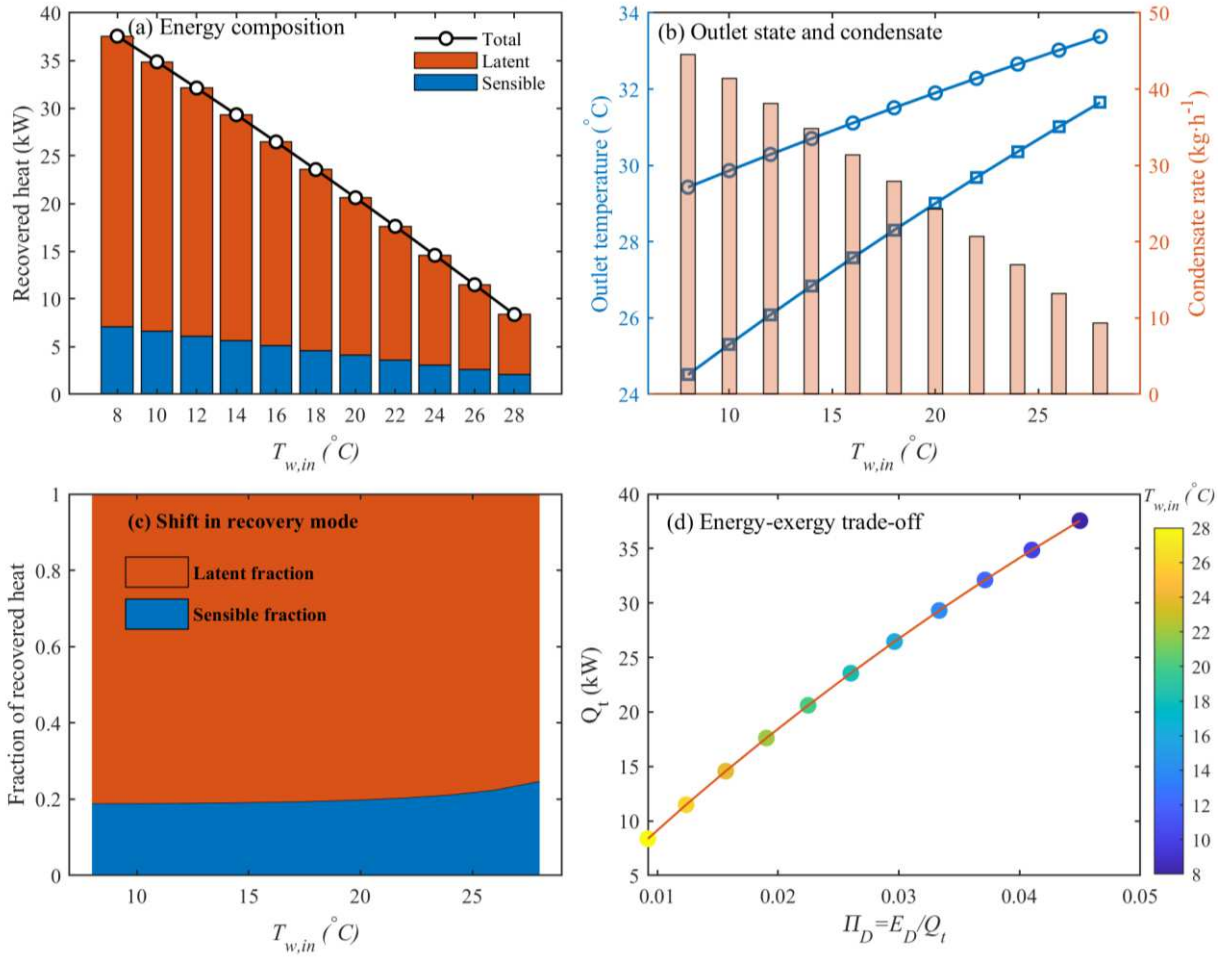

Figure 4. Influence of inlet groundwater temperature on (a) sensible, latent and total recovered heat, (b) outlet states and condensate production, (c) sensible/latent energy fractions, and (d) the energy–exergy trade-off.

The outlet-state and condensate-rate responses in Fig. 4(b) show that a lower groundwater temperature simultaneously reduces the outlet air temperature and increases moisture removal. However, the energy-quality penalty also rises. As $T_{w,in}$ decreases from 28 to 8 °C, the overall exergy destruction increases from roughly 0.08 to 1.69 kW. The energy–exergy trajectory in Fig. 4(d) therefore reveals a genuine trade-off: operating at a lower water temperature increases first-law recovery but also increases the irreversibility generated by finite temperature differences and vapor-transfer disequilibrium. The appropriate design objective is consequently not the minimum achievable water temperature, but a matched cold-source condition that provides sufficient condensation without unnecessary exergy destruction.

5.4 Influence of inlet air humidity

Increasing inlet relative humidity changes the process in a fundamentally different way from lowering the water temperature. As ϕ_{in} increases from 0.60 to 0.96 at fixed $T_{a,in}$=35 °C and $T_{w,in}$=18 °C, total recovery increases from approximately 12.7 to 25.6 kW, while the increase is dominated by the latent component. The condensate production therefore rises strongly with humidity, even though the outlet dry-bulb temperature does not decrease proportionally. This confirms that dry-bulb cooling alone is a poor performance indicator for near-saturated mine return air.

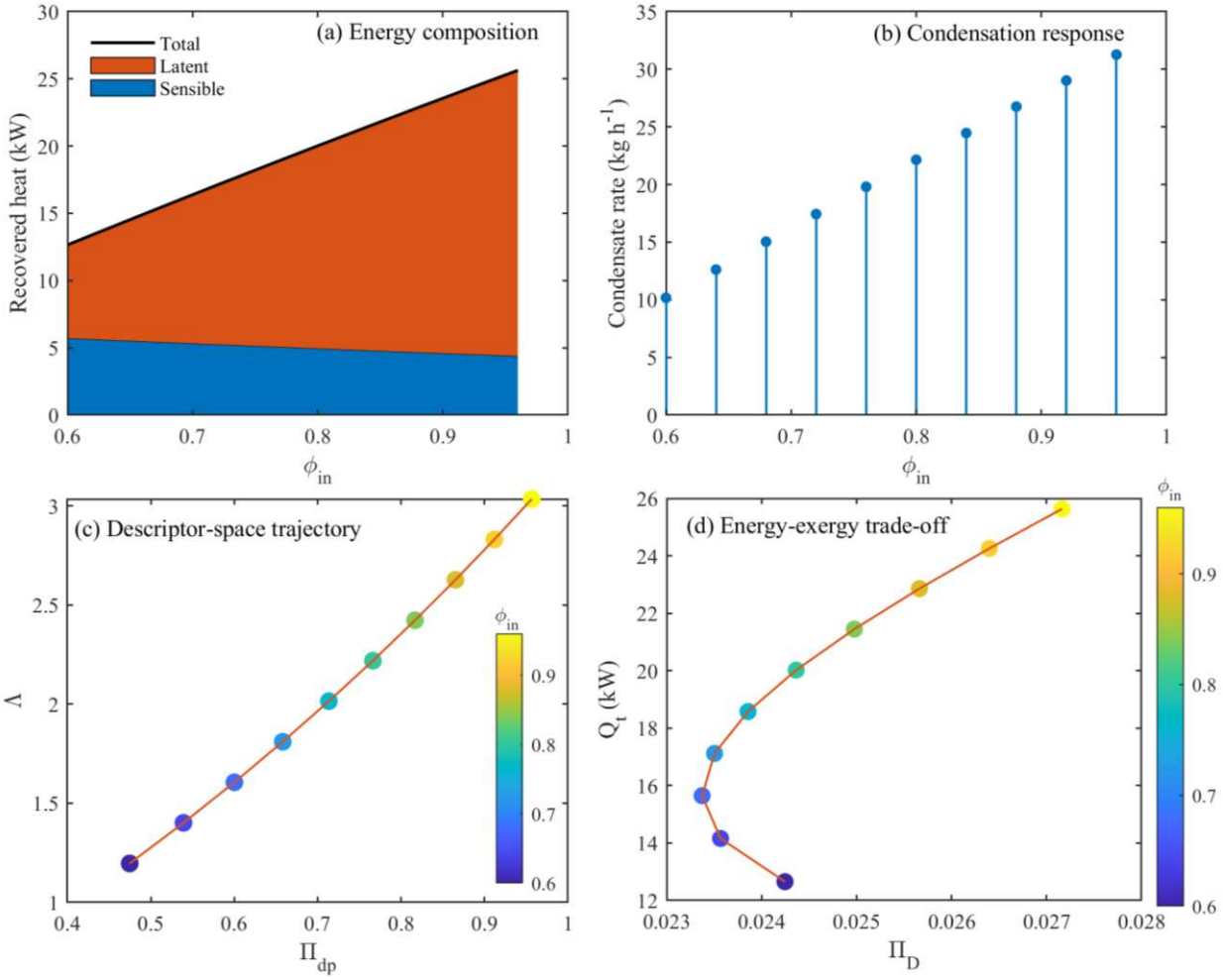

Figure 5. Influence of inlet relative humidity on (a) sensible, latent and total heat recovery, (b) condensate rate, (c) trajectory in the Π_{dp}–Λ descriptor space, and (d) the energy–exergy trade-off.

The descriptor-space trajectory in Fig. 5(c) provides a compact interpretation of the transition. Both the dew-point-crossing number Π_{dp} and the latent-potential ratio Λ increase as the inlet humidity rises, moving the system away from a weak-condensation state and toward a strongly latent-dominated regime. At the same time, Fig. 5(d) shows that the exergy-destruction ratio also increases. A larger moisture load therefore increases

recoverable enthalpy, but the additional recovered energy is accompanied by a greater second-law penalty. This result is especially relevant to deep mines, where high relative humidity can make the enthalpy load very large even when the dry-bulb temperature is only moderately elevated.

5.5 Thermodynamic regime descriptors

The inlet maps in Fig. 6 separate the two thermodynamic prerequisites for strong condensation. Π_{dp} measures the extent to which the water temperature lies below the inlet-air dew-point scale, whereas Λ compares the potential latent load associated with condensation against the sensible cooling potential. The $\Pi_{dp} = 0$ contour is the inlet dew-point-crossing boundary. Conditions above this boundary have a thermodynamic tendency to condense water vapor, while increasingly positive Π_{dp} indicates progressively deeper dew-point crossing. In contrast, $\Lambda > 1$ identifies conditions for which the available latent condensation potential exceeds the sensible cooling potential.

The two boundaries do not coincide because condensation onset and latent dominance are different physical questions. A state can cross the dew point while still having only a modest latent contribution, whereas near-saturated air combined with sufficiently cold groundwater can simultaneously produce large Π_{dp} and Λ. The descriptor maps can therefore be used as a rapid pre-screening tool before solving the full coupled model.

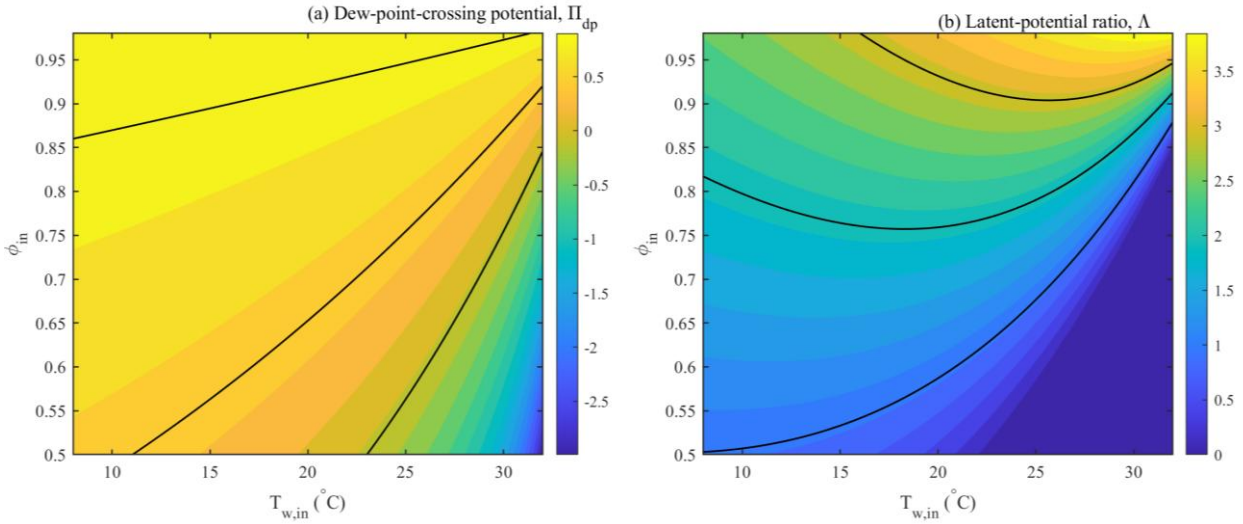

Figure 6. Thermodynamic inlet regime descriptors at $T_{a,in}$=35 °C: (a) dew-point-crossing number Π_{dp} and (b) latent-potential ratio Λ as functions of inlet groundwater temperature and inlet relative humidity.

5.6 Two-parameter operating maps from the coupled model

Figure 7 extends the inlet descriptors to response quantities obtained from the coupled transport model. The condensation-zone fraction χ_c identifies how much of the nominal contact length remains thermodynamically active for condensation. The latent-dominance factor Π_L distinguishes sensible-dominated and latent-dominated recovery, while $\dot{Q}_t$ and Π_D show the simultaneous first- and second-law consequences. Low groundwater temperature and high inlet humidity act cooperatively: they expand the condensation-active region and increase total enthalpy recovery, but they also move the process toward stronger latent dominance and greater exergy degradation. In Fig. 7(c) and (d), non-positive heat-recovery states are masked because $\Pi_D = \dot{E}_D/\dot{Q}_t$ is not a meaningful recovery metric when $\dot{Q}_t \leq 0$.

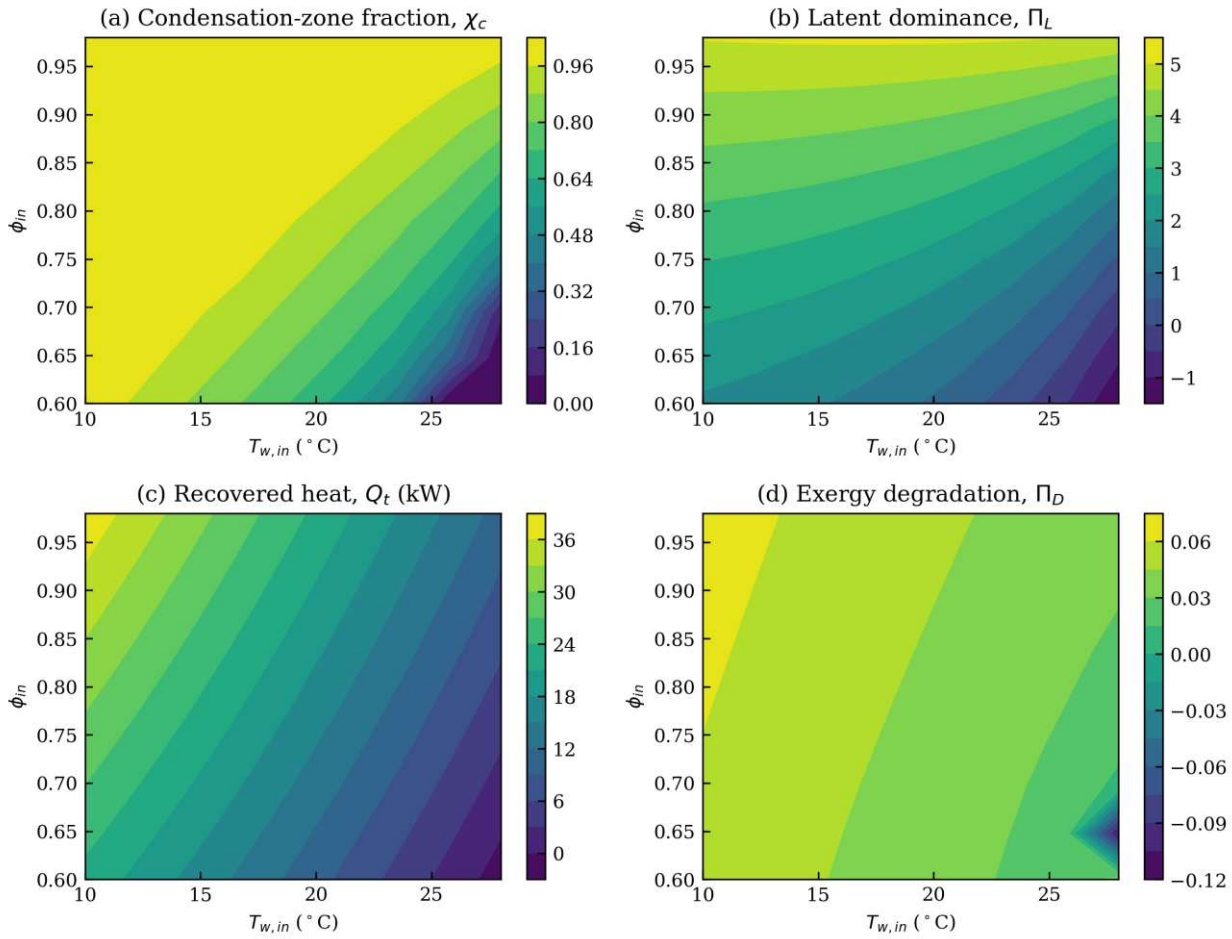

Figure 7. Two-parameter operating maps of the coupled model: (a) condensation-zone fraction χ_c, (b) latent-dominance factor Π_L, (c) total recovered heat $\dot{Q}_t$, and (d) exergy-degradation number Π_D as functions of inlet groundwater temperature and inlet relative humidity. Non-positive heat-recovery states are masked in panels (c)–(d).

5.7 Pareto trade-off between heat recovery and exergy destruction

The combined operating space is projected onto the recovered-heat–exergy-destruction plane in Fig. 8. The non-dominated points form a Pareto envelope: moving along this envelope toward larger $\dot{Q}_t$ necessarily requires accepting a larger $\dot{E}_D$, whereas points located away from the envelope are thermodynamically inferior because another operating condition can provide equal or greater heat recovery with lower exergy destruction. The Pareto representation converts the qualitative statement that "stronger recovery causes greater irreversibility" into a design criterion that can be used to screen operating conditions without imposing an arbitrary weighting factor between energy quantity and energy quality.

For engineering design, the preferred operating point need not be the maximum-$\dot{Q}_t$ end of the Pareto envelope. Mine-specific constraints such as available groundwater flow, pumping power, fan power, corrosion risk, water treatment, droplet carryover, and downstream humidity requirements should determine where on the envelope the system is operated. The thermodynamic model therefore provides the feasible performance boundary, while auxiliary energy consumption and site constraints determine the final design choice.

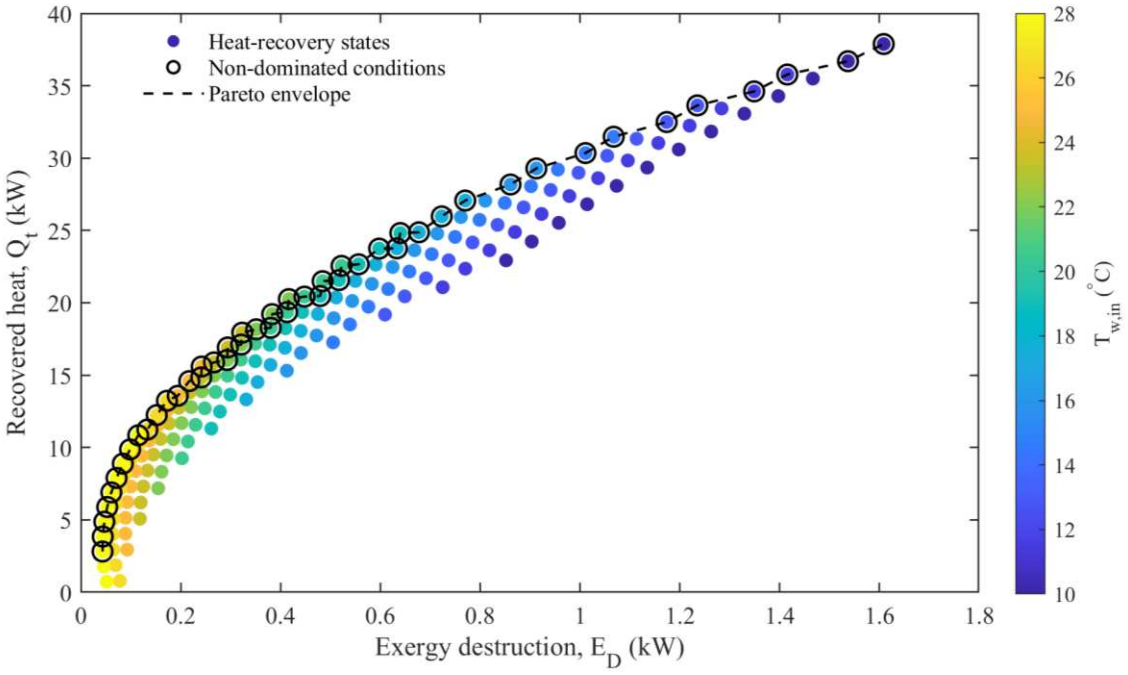

Figure 8. Energy–exergy Pareto map for the combined inlet-groundwater-temperature and inlet-humidity operating space. Circled points denote non-dominated conditions.

5.8 Response-based operating-regime map and engineering implications

Figure 9 translates the continuous model response into four operating regimes using explicit response thresholds. A case is classified as weak/no condensation when χ_c<0.05; when χ_c≥0.05, Π_L<1 denotes mixed sensible–latent transfer, 1≤Π_L<3 denotes latent-dominated transfer, and Π_L≥3 denotes strongly latent-dominated transfer. The boundary Π_L=1 has a direct physical meaning because latent and non-latent contributions are equal. The value χ_c=0.05 is an engineering/numerical activity tolerance, whereas Π_L=3 is used only as an operational visualization threshold for a strongly latent-dominated response and is not proposed as a universal critical value. The classification is therefore response-based rather than being defined solely by the inlet dew point; inlet dew-point crossing alone does not guarantee that condensation remains active over a meaningful fraction of the contact length.

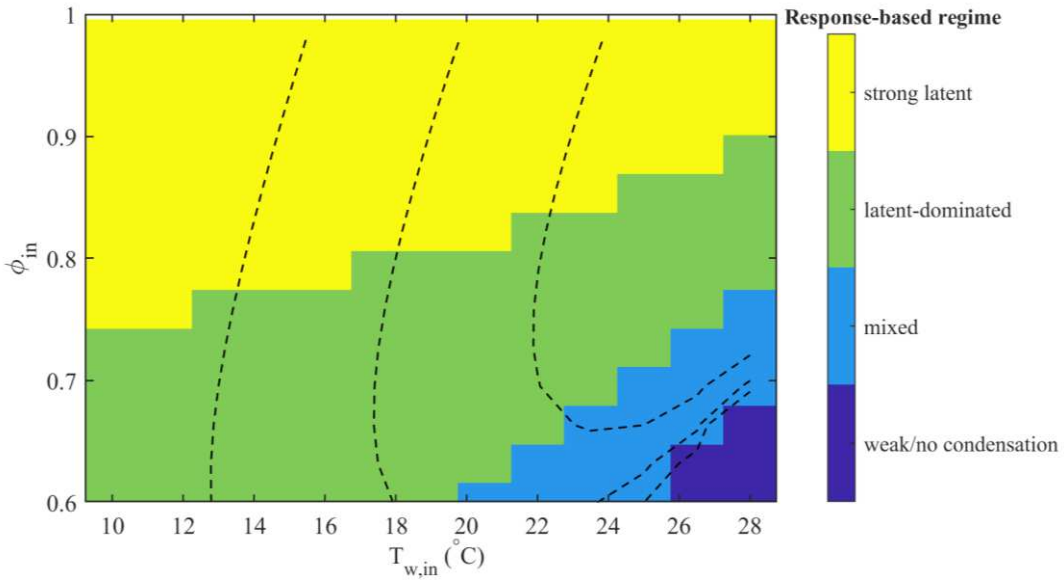

Figure 9. Response-based operating-regime map for coupled heat and moisture recovery. Regimes are defined by χ_c=0.05, Π_L=1 and the operational visualization threshold Π_L=3; dashed contours indicate the variation in exergy-degradation level.

Three engineering implications follow. First, direct-contact mine-water recovery should be designed around the thermodynamically active condensation length rather than the total geometrical length; staged water distribution or renewal of the cold source can be more effective than simply enlarging downstream contact area. Second, groundwater temperature and air humidity must be considered jointly because they determine whether the device operates in a mixed or latent-dominated regime. Third, the optimal condition should be selected close to the Pareto envelope and away from regions where additional heat recovery is accompanied by a disproportionate increase in exergy destruction. For actual wetted-string-grid, spray or packed-contact devices, the present framework should be coupled with apparatus-specific *Nu*/*Sh* correlations, pressure-drop models and measured interfacial-area characteristics.

6. Conclusions

A thermodynamically consistent one-dimensional model was developed for direct contact between deep-mine humid return air and low-temperature groundwater under dew-point-crossing conditions. The formulation incorporates local signed two-film heat and mass transfer, explicit augmentation of the liquid flow by condensate, the finite thermal capacity of groundwater, and moist-air exergy analysis. Comparison with the ASHRAE parallel-flow air-washer benchmark gives a mean absolute relative deviation of 10.1% for four outlet descriptors without fitting the outlet states, while available direct-contact experimental data reported in the literature support the predicted response trends. The main conclusions are as follows.

(1) Dew-point crossing is governed by the local thermodynamic state rather than by a single inlet criterion. Under the baseline condition of 35 °C, 90% RH inlet air and 18 °C groundwater, the inlet dew-point temperature is approximately 33.1 °C and the process is strongly condensation dominated. The total heat recovery reaches approximately 23.6 kW, of which about 19.0 kW is contributed by latent heat. Thus, an analysis based solely on dry-bulb temperature reduction substantially underestimates the energy recovered from high-humidity mine return air.

(2) Heat and moisture transfer exhibit pronounced spatial localization. The vapor-pressure driving force and condensation rate are highest near the contactor inlet and decrease rapidly as the air approaches the local interfacial equilibrium state. Approximately 82.6% of the total moisture removal and 92.9% of the cumulative exergy destruction occur within the first 40% of the reference contact length. This upstream concentration indicates that increasing the geometric contact length does not necessarily produce a proportional improvement in recovery performance and provides a physical basis for staged cold-water distribution and more effective utilization of the active contact region.

(3) Accounting for the finite thermal capacity of groundwater fundamentally changes the attainable recovery limit. For the baseline case, the common finite-source equilibrium temperature is approximately 28.9 °C. The corresponding finite-source enthalpy effectiveness is about 0.95, whereas the conventional effectiveness referenced to the inlet groundwater temperature is only about 0.35. The finite-source equilibrium therefore provides a physically attainable upper bound and avoids the overly optimistic limit implied by treating groundwater as an infinite-temperature reservoir.

(4) Lower groundwater temperature and higher inlet humidity jointly enhance condensation and total heat recovery, while simultaneously increasing thermodynamic irreversibility. The operating maps show a progressive transition from mixed sensible–latent transfer to latent-dominated operation as the condensation potential increases. Sensitivity analysis further shows that the principal regime structure and finite-source conclusions remain robust to variations in the effective transfer conductances, although absolute device-scale predictions depend on apparatus-specific transport coefficients. The resulting heat-recovery–exergy-destruction relationship therefore represents a trade-off rather than a single-objective optimum, and practical operating conditions should be selected near the Pareto-efficient region while considering groundwater availability, pumping and fan power, outlet humidity, and pressure-drop constraints. Future work should establish geometry-specific heat- and mass-transfer correlations and experimentally validate the predicted condensation-regime boundaries.

CRediT authorship contribution statement

All authors contributed to the writing of the paper and provided critical input that helped shape the research, analysis, and paper. **Huang M H:** Conceptualization, formal analysis, writing original draft, study conception and design, analysis and interpretation of results, draft manuscript preparation. **Jin H X:** carried out the research. **Yang K**: designed the research, supervised the work. **Li C:** conceived the research. **Xu A X:** carried out the research. **Chen S Q:** carried out the research.

Declaration of conflicting interests

The author(s) declared no potential conflicts of interest with respect to the research, authorship, and/or publication of this article.

Data availability

Data will be made available on request.

Acknowledgments

This study was supported by the Excellent Youth Project of Scientific Research of Hunan Provincial Department of Education(25B0521), by the Key Science and Technology Projects in Transportation Industry Funded by Ministry of Transport, China (2021-MS5-126).

References

[1] Ding D, Du C, Lin Y, Chang B, Wang Y. Thermal environment assessment of deep mine based on analytic hierarchy process and fuzzy comprehensive evaluation. *Case Studies in Thermal Engineering*. 2020;19:100618.

[2] You B, Chen Y, Yang M, Gao K, Cui D, Lu M. Management of thermal hazards in deep mines in China: applications and prospects of mine cooling technology. *Water*. 2024;16(16):2347.

[3] Wang K, Li Q, Wang J, Yang S. Thermodynamic characteristics of deep space: hot hazard control case study in 1010-m-deep mine. *Case Studies in Thermal Engineering*. 2021;28:101656.

[4] Sasmito AP, Kurnia JC, Birgersson E, Mujumdar AS. Computational evaluation of thermal management strategies in an underground mine. *Applied Thermal Engineering*. 2015;90:1144–1150.

[5] Guo P, Wang Y, Duan M, Pang D, Li N. Research and application of methods for effectiveness evaluation of mine cooling system. *International Journal of Mining Science and Technology*. 2015;25(4):649–654.

[6] Xiang J, Bi P, Pisaniello D, Hansen A. Health impacts of workplace heat exposure: an epidemiological review. *Industrial Health*. 2014;52(2):91–101.

[7] Devres YO. Psychrometric properties of humid air: calculation and use of psychrometric charts. *Applied Energy*. 1994;48(1):1–18.

[8] Luo Y, Yang H, Lu L, Qi R. A review of the mathematical models for predicting the heat and mass transfer process in the liquid desiccant dehumidifier. *Renewable and Sustainable Energy Reviews*. 2014;31:587–599.

[9] Zhang L, Song X, Zhang X. Theoretical analysis of exergy destruction and exergy flow in direct contact process between humid air and water/liquid desiccant solution. *Energy*. 2019;187:115976.

[10] Qureshi BA, Zubair SM. Application of exergy analysis to various psychrometric processes. *International Journal of Energy Research*. 2003;27(12):1079–1094.

[11] Gandhidasan P. A simplified model for air dehumidification with liquid desiccant. *Solar Energy*. 2004;76(4):409–416.

[12] Luo Y, Yang H, Lu L. Liquid desiccant dehumidifier: development of a new performance prediction model based on CFD. *International Journal of Heat and Mass Transfer*. 2014;69:408–416.
[13] Min Y, Shi W, Shen B, Chen Y, Yang H. Enhancing the cooling and dehumidification performance of indirect evaporative cooler by hydrophobic-coated primary air channels. *International Journal of Heat and Mass Transfer*. 2021;179:121733.
[14] Zhang S, Wei X, Cheng Q. Theoretical and experimental research on heat and mass transfer process of positive-pressure condensation dehumidification for humid air. *International Journal of Refrigeration*. 2024;168:61–75.
[15] Feng X, Jia Z, Liang H, Wang Z, Wang B, Jiang X, Cao H, Sun X. A full air cooling and heating system based on mine water source. *Applied Thermal Engineering*. 2018;145:610–617.
[16] Yang D, Peng K, Zheng Y, Chen Y, Zheng J, Wang M, Chen S. Study on the characteristics of coal and gas outburst hazard under the influence of high formation temperature in deep mines. *Energy*. 2023;268:126645.
[17] Wang C, Zhao H, Cheng L, Li G, Fan Y, Jiang M, Hao Y, Shao K. Layout and parameter analysis of the cooling system with mine water as cold source in Linglong gold mine. *Geofluids*. 2023;2023:1–12.
[18] Chen G. Field experimental study on the cooling effect of mine cooling unit. *International Journal of Mining Science and Technology*. 2013;23(5):645–651.
[19] Poredoš P, Petelin N, Vidrih B, Žel T, Ma Q, Wang R, Kitanovski A. Condensation of water vapor from humid air inside vertical channels formed by flat plates. *iScience*. 2022;25(1):103556.
[20] Poškas R, Širvydas A, Salem M, Poškas P, Jouhara H. Experimental investigation of water vapor condensation from hot humidified air in serpentine heat exchanger. *International Journal of Heat and Mass Transfer*. 2024;221:125068.
[21] Poškas R, Širvydas A, Salem M, Jouhara H. Experimental investigation of humidified air condensation in different rows of serpentine heat exchanger: cooling water flow rate effect. *Thermal Science and Engineering Progress*. 2024;54:102814.
[22] Hu W, Ma A, Guan Y, Cui Z, Zhang Y, Wang J. Experimental study of the air side performance of fin-and-tube heat exchanger with different fin material in dehumidifying conditions. *Energies*. 2021;14(21):7030.
[23] Zhang L, Liu X, Jiang Y. Exergy analysis of parameter unmatched characteristic in coupled heat and mass transfer between humid air and water. *International Journal of Heat and Mass Transfer*. 2015;84:327–338.
[24] Alhazmy MM. Power estimation for air cooling and dehumidification using exergy analysis. *International Journal of Exergy*. 2006;3(4):391–401.
[25] Zhang L, Liu X, Jiang J, Jiang Y. Exergy calculation and analysis of a dehumidification system using different desiccants. *Energy and Buildings*. 2014;82:430–440.
[26] Ge F, Wang C. Exergy analysis of dehumidification systems: a comparison between condensing dehumidification and desiccant wheel dehumidification. *Energy Conversion and Management*. 2020;224:113340.
[27] Rogala Z, Kolasiński P. Exergy analysis of fluidized desiccant cooling system. *Entropy*. 2019;21(8):757.
[28] Zhai Y, Zhao X, Dong Z. Research on performance optimization of gravity heat pipe heat exchanger in mine return air heat recovery. *Energies*. 2022;15(22):8449.
[29] Ghoreishi-Madiseh SA, Kalantari H, Kuyuk AF, Sasmito AP. A new model to analyze performance of mine exhaust heat recovery systems with coupled heat exchangers. *Applied Energy*. 2019;256:113922.
[30] Buck AL. New equations for computing vapor pressure and enhancement factor. *Journal of Applied Meteorology*. 1981;20(12):1527–1532.
[31] ASHRAE. *2021 ASHRAE Handbook—Fundamentals*, Chapter 6: Mass Transfer. SI ed. Atlanta, GA: American Society of Heating, Refrigerating and Air-Conditioning Engineers; 2021.
[32] Yoo SY, Kwon HK. An experimental study on the performance of air/water direct contact air conditioning system. *KSME International Journal*. 2004;18(6):1002–1009. doi:10.1007/BF02990872.
[33] Karameldin A, Shouman LA, Fadel DA. Humidification-dehumidification spray column direct contact condenser—Part II: Experimental co-current flow. *Desalination and Water Treatment*. 2018;132:20–29. doi:10.5004/dwt.2018.23061.